

## Why Do Nanotubes Grow Chiral?

Vasilii I. Artyukhov,<sup>\*</sup> Evgeni S. Penev,<sup>\*</sup> and Boris I. Yakobson<sup>†</sup>

*Department of Materials Science and NanoEngineering, Rice University, Houston, TX 77005, USA*

(Dated: February 19, 2022)

Carbon nanotubes (CNT) hold enormous technological promise. It can only be harnessed if one controls in a practical way the CNT chirality, the feature of the tubular carbon topology that governs all the CNT properties—electronic, optical, mechanical. Experiments in catalytic growth over the last decade have repeatedly revealed a puzzling strong preference towards minimally-chiral (near-armchair) CNT, challenging any existing hypotheses and turning chirality control ever more tantalizing, yet leaving its understanding elusive. Here we combine the CNT/catalyst interface thermodynamics with the kinetic growth theory to show that the unusual near-armchair peaks emerge from the two antagonistic trends: energetic preference towards achiral CNT/catalyst interfaces vs. faster growth of chiral CNT. This narrow distribution is profoundly related with the peaked behavior of a simple function,  $x e^{-x}$ .

The broad interest in carbon nanotubes (CNT), unceasing since their first clear observation [1], has been fueled by possible technological applications derived from their unique fundamental properties [2–4]. All of the latter are in turn determined by the helical fashion of folding a tube, specified by the chiral angle  $\chi$  between its circumference and the zigzag motif in the honeycomb lattice of atoms, with  $\chi = 0^\circ$  and  $\chi = 30^\circ$  for the achiral types, zigzag and armchair. Alternatively, a pair of chiral indices  $(n, m)$  is commonly used, the integer components of the circumference-vector [2]. In spite of such defining role of chirality, most synthetic methods yield a broad distribution with mixed properties. To achieve control of the CNT type remains a great challenge; what physical mechanisms determine the chirality distribution, and even why the nanotubes grow chiral is still unsettled.

Although the discovery paper by Iijima [1] has already suggested one key, connecting the tube ability to grow with the kinks at its end and the screw dislocation model, yet it took nearly two decades till the first equation [5] related the speed of growth and chirality,  $R \sim \sin \chi$ . It should further be useful to think, in hindsight, of the probable causes of such delay. Besides the difficulties of determining chirality in experiment, in theory it was ambiguous whether the chiral angle must be measured from the zigzag (as  $\chi$ ) or perhaps from the armchair (as  $\chi^- \equiv 30^\circ - \chi$ ) direction. While either choice appears valid from pure symmetry standpoint, it changes the kinetic prediction to the opposite, and thus one stumbles upon an immediate contradiction. Another diversion was due to simple thermodynamic argument that the lower energy of the tube edge, rather than its kinetic advantage of having kinks, must determine the dominant CNT type, pointing towards the armchair tubes, especially (10, 10) broadly discussed by Smalley *et al.* [6].

This situation, together with recent advances in synthesis showing in several cases very narrow chiral distributions [7–9], poses a compelling question of which factors—thermodynamic preference to lower energy, or kinetic preference of higher speed—play major role in defining the distribution of CNT product. The true answer appears “both”, and the analysis below shows how the subtle interplay of these physical factors defines the more probable chirality choices. In particular, it explains why at lower temperature on solid cata-

lyst particles the yield is peaked near armchair type  $(n, n-1)$ , never exactly armchair, although quite close.

The evolution of chemical vapor deposition (CVD) techniques and chirality characterization methods [10] has led to improvements in chiral selectivity [7–9, 11–16], eventually reaching  $> 50\%$  fraction for a single CNT type and  $\sim 90\%$  for semiconducting tubes [9]. More intuitive strategies such as post-growth selection [17, 18], rational synthesis [19–21], or seeding [22–24] do, in principle, offer great selectivity but lack the scalability of CVD. Further improvements of the latter direct synthesis techniques thus call for better understanding of the growth process. Yet its mechanism and especially the causes behind its occasional success in chiral preference remain puzzling. In modeling efforts, direct molecular dynamics (MD) simulations, although invaluable in many respects, generally fail to produce non-defective CNT structures of a well-defined diameter and recognizable chirality, regardless of the precision of interatomic potentials—from classical [25–28] to tight-binding [29, 30] and density functional theory (DFT) [31]. This is caused by the short time-scale due to sheer computational limitations. It is clear that a physical theory bridging the gap between atomistic dynamics and macroscopic scales is needed to interpret both the experiments and simulations.

At proper conditions, the nanotubes *nucleation* occurs, with probability  $N_{n,m}$  of certain chiral type. It is followed by the steady carbon accretion by each tube, with its *growth rate*  $R_{n,m}$ . After some time, the fraction of the tubes of chirality  $(n, m)$ , i.e., their relative abundance  $A_{n,m}$  in the accumulated material, is determined by the product of both these factors [32] as  $A_{n,m} = N_{n,m} \cdot R_{n,m}$ . Using instead of the chiral indexes the tube diameter  $d$  and chiral angle  $\chi$  one has,  $A(\chi, d) = N(\chi, d) \cdot R(\chi, d)$ . Below we explore the physical mechanisms defining the right-hand side, in particular the case of solid catalyst with rigid shape, which yields sharp chiral angle selectivity in  $A(\chi, d)$ , as empirical evidence suggests.

During **nucleation**, as carbon atoms attach to a nascent CNT nucleus, adding new hexagonal and pentagonal rings to it, the chirality of a CNT becomes permanently “locked in” when the final 6<sup>th</sup> pentagon is added to the hemispherical cap. From this 6-pentagon nucleus a cylindrical CNT struc-

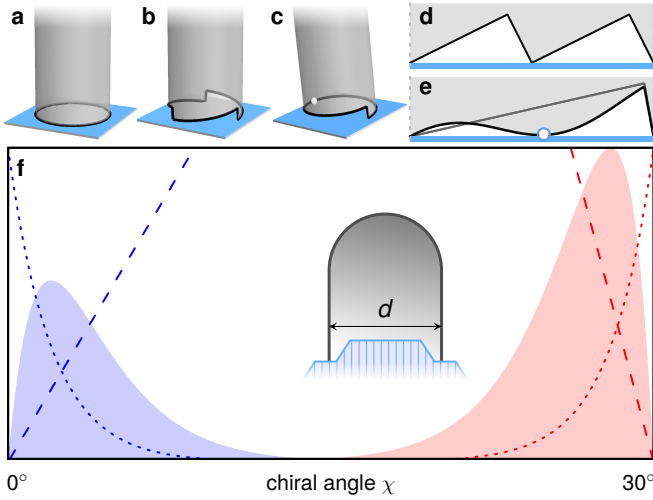


**Fig. 1. Continuum model of the CNT-catalyst system.** Schematic representation of (a) achiral, (b) multiple-kink chiral, and (c) single-kink chiral CNT on a flat substrate. Unrolled CNT-substrate interfaces for (d) two-kink and (e) single-kink nanotubes show the nanotube tilt off the vertical, reducing the edge-substrate gap; the white dot in (c) and (e) marks the contact point. The abundance distributions  $A(\chi) \sim \chi e^{-\chi}$  computed as the product of nucleation (dotted) and growth rate (dashed) terms are shown in (f) for near-Z (blue) and near-A (red) chiralities. The inset illustrates a nascent CNT of diameter  $d$  on a solid catalyst.

ture can further grow by adding only hexagons, in a periodic fashion. The free energy of the critical nucleus contains two contributions,  $G^* = G_{\text{cap}} + \Gamma$ . The first one,  $G_{\text{cap}}$ , originates from the “elastic” energy of cap *per se* and does not depend on  $\chi$  [33]. The second term  $\Gamma$  represents the contact interface between the  $sp^2$ -carbon lattice edge and the metal catalyst, and does contain chirality dependence since the edge energy  $\gamma(\chi)$  varies with the crystallographic orientation and  $\Gamma(\chi, d) \equiv \pi d \gamma(\chi)$ . Whereas previous studies on edge energetics [34] assumed either vacuum or a liquid-like catalyst that fully adapts to the edge shape, chiral-selective CVD growth is usually reported at comparatively low temperatures [8, 9] when the catalyst particle is solid [9]. Accordingly, the metal side of the interface is rather a rigid atomic plane, and the structure of this interface affects both the energy of the nucleus and the subsequent insertion of new C-atoms during growth.

Before discussing the details of atomistic study, it is useful to explore the key ideas in terms of simpler **continuum model**, which not only offers valuable insight but is even able to make accurate overall predictions. In **Fig. 1** inset, the CNT is in contact with the catalyst which is represented locally as a continuous plane corresponding to an atomic terrace in a solid particle. The CNT is also continuous, but the kinks around its edge are retained according to the tube chirality, **Fig. 1a–c**. These kinks cause the gaps between the substrate and the CNT, shown in **Fig. 1b–c** for  $(n, 3)$  and  $(n, 1)$  tubes, with an associated energy penalty, relative to the tight contact in case of achiral tube in **Fig. 1a**. For the hexagonal lattice of CNT

the two fundamental achiral edges—armchair (A) and zigzag (Z)-form tight low-energy contacts. The interface energy for chiral tubes is higher, roughly in proportion with the number of kinks, which raises linearly with  $\chi$  for near-Z tubes, or with  $\chi^-$  for near-A tubes. In other words,  $\gamma(x) \approx \gamma + \gamma' \cdot x$ , where  $x$  is the angular deviation from the achiral direction: near the Z-type  $x = \chi$ ,  $\gamma = \gamma_Z \equiv \gamma(0^\circ)$ , and  $\gamma' = \partial\gamma/\partial\chi|_{\chi=0^\circ}$ , or near the A-type  $x = \chi^-$ ,  $\gamma = \gamma_A \equiv \gamma(30^\circ)$ , and  $\gamma' = -\partial\gamma/\partial\chi|_{\chi=30^\circ}$ .

Since  $\gamma(x)$  is largest in the intermediate range of  $\chi \approx 15^\circ$ , such tubes are unlikely to nucleate, and one should focus on just the neighborhoods of Z and A chiralities. Then we write (omitting for brevity the  $k_B T$  factor, wherever obvious):

$$N(\chi, d) \propto e^{-G^*} \propto e^{-\pi d(\gamma + \gamma' \cdot x)}. \quad (1)$$

The essential result here is that the nucleation probability falls rapidly as  $e^{-\beta \cdot x}$  with chiral angle  $x$  and  $\beta = \pi d \gamma' / k_B T$ . A distinction for single-kink cylinders, representing the nanotubes  $(n, 1)$  and  $(n, n-1)$ , should be noted. Their symmetry allows them to tilt in the vertical plane, improving the interface contact. **Fig. 1d–e** illustrates it by “unrolling” the CNT-substrate interface area for two-kink and single-kink tubes. In the latter case, the effect of tilt leads to a reduction of the tube-substrate separation, appearing as a sinusoid along the circumference as shown in **Fig. 1e**, enabling a substantial closure of the gap between substrate and tube edge, recovering up to as much as 70% of the energy penalty according to our estimates.

For the **growth rate** term  $R(\chi, d)$  we augment the screw dislocation model [5] by including the kinks created by thermal fluctuations on A and Z edges [35], and accounting for the energy penalty  $\sim 1/d^2$  from the wall curvature. In the liquid-catalyst model, when the metal adapts to the CNT edge with a one-to-one termination, calculations suggest that the cost  $E_A$  to create a pair of kinks on an A edge is zero, and consequently  $R \propto \chi$  [5]. However, on a solid surface, creating a pair of kinks destroys the perfect contact between the CNT and substrate, costing energy. Therefore  $E_A$  has a noticeable magnitude, and the dependence becomes bimodal with minima at the A and Z ends of the chiral angle range, and a maximum at the magic angle of  $19.1^\circ$  [35, 36]. The final expression, linearized near the A and Z bounds of chirality reads as follows,

$$R(\chi, d) \propto \pi d e^{-2C/d^2} (x + e^{-E}), \text{ nearly as } \propto x, \quad (2)$$

where  $C = 3.9 \text{ eV} \cdot \text{\AA}^2/\text{atom}$  is the bending rigidity of graphene [37]. The term  $x$  in parentheses corresponds to the density of geometry-imposed kinks, proportional to the vicinal-edge angular deviation from the main achiral direction, and the term  $e^{-E}$  (typically small) represents the additional fluctuational kinks. The free energy barriers for the initiation of a new atomic row on A or Z edge are  $E = E_Z$  near the Z-type where  $x = \chi/\sqrt{3}$ , or  $E = E_A$  near the A-type where  $x = \chi^-$ .

Multiplying together the nucleation and growth terms presents the key to understanding the observed selectivity for near-A chiralities [9]. At a given diameter,

$$A(\chi) = N(\chi)R(\chi) \sim \chi e^{-\chi}, \quad (3)$$

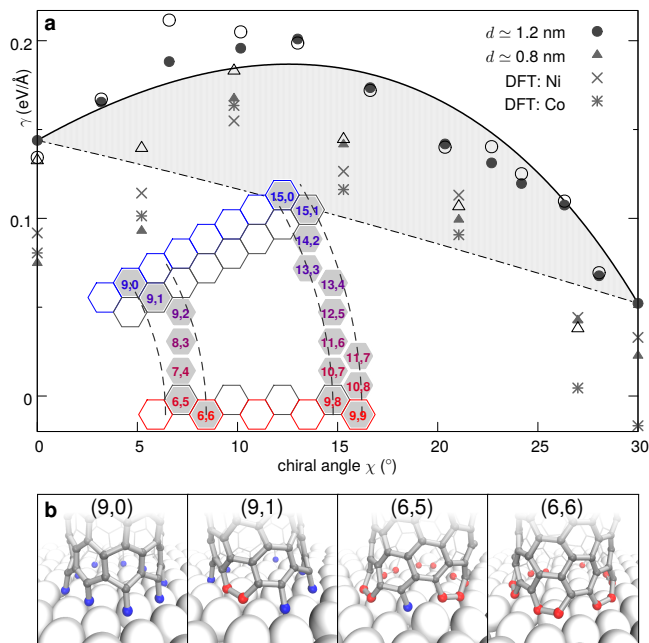


**Fig. 2. Chirality-dependent CNT–catalyst contact energies, governing the nucleation.** (a) Interface energies calculated with MD (circles and triangles) and fitted with analytical expression (solid line) for two CNT sets (inset; dashed arcs denote the range of diameter variation in each set). Static DFT calculations on Ni and Co are also shown. Open and filled symbols denote regular (hexagonal) and Klein Z edge structures—see sample atomistic structures (b). The dash-dotted line corresponds to liquid catalyst case. In (b) the blue and red atoms highlight the Z- and A-edges, respectively.

a function with a sharp peak near zero (or near  $30^\circ$ ). This is the essential result of our continuum consideration. Fig. 1f illustrates this peaked distribution character. The two distributions for near-Z (blue) and near-A (red) chiral angles are plotted assuming equal interface energies and growth barriers:  $\gamma_A = \gamma_Z$ ,  $E_A = E_Z$ . However, if either A or Z has a lower energy, the opposite peak distribution is additionally penalized by  $e^{-\Delta\Gamma}$ , with  $\Delta\Gamma = \Gamma_Z - \Gamma_A$  on the order of eV, and then one would expect to observe only one side of the distribution. These continuum-model predictions turn out to be remarkably robust. To see this, below we present the atomistic calculations of the relevant quantities, and proceed to simulate example CNT type distributions.

**Atomistic computations** were performed using a flat Ni(111) slab to represent the solid catalyst. We used a classical force-field MD sampling complemented with static DFT computations. MD calculations were performed using the canonical ( $NVT$ ) ensemble with the ReaxFF force field [38, 39] as implemented in the LAMMPS simulation package [40, 41]. DFT calculations were performed with the local spin density approximation using the QUANTUM ESPRESSO package [42].

To investigate the chiral selectivity of nucleation, two sets of CNT are chosen, with  $d \approx 0.8$  and  $1.2$  nm, to include the prominent in experiments (6,5) and (9,8) CNT. Fig. 2a shows

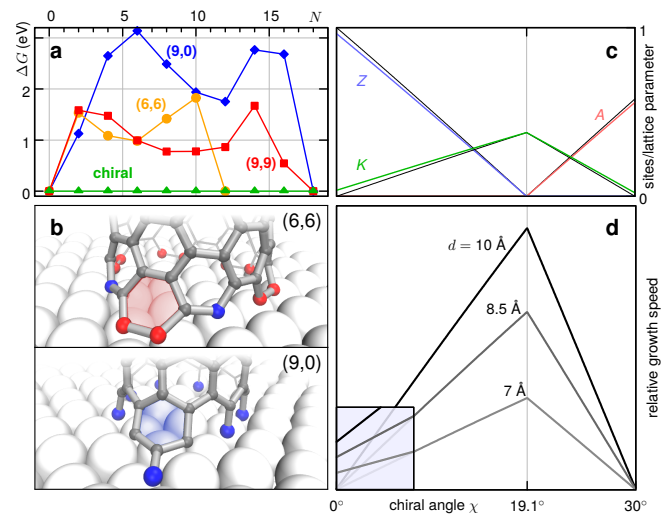


**Fig. 3. Chirality-dependent growth rate of CNT.** (a) Free energy profiles during the growth of a new ring of hexagons on (red, orange) A and (blue) Z edges as a function of number of added atoms  $N$ . The green line corresponds to barrierless chiral edge growth. (b) The atomic configurations after first dimer addition,  $N = 2$ . (c) Linear density of different site types on CNT edges as a function of chiral angle. (d) The resulting CNT growth rate as a function of chiral angle for several diameters (inset shows the effect of thermal kinks).

the calculated CNT–substrate interface energies. The atomistic structures for the (9,0), (6,5), and (6,6) CNT are shown in Fig. 2b, where the tilting of the (6,5) and (9,1) CNT to reduce the interface energy is seen clearly. We found that for the smaller-diameter set, for near-Z edges a Klein structure with dangling C atoms [43] is favored over the standard closed-hexagons, whereas the larger-diameter set shows little preference either way. All data display the same qualitative behavior conforming to the above discussion, and are generally in good quantitative agreement. Both bounds of the chiral angle range (achiral CNT) are energy minima, and the energy is higher for Z than for A tubes. The curves show the fit of  $\gamma(\chi)$  using the analytical expression from earlier work [34] for solid and liquid-like cases.

Our computations pertaining to the growth kinetics are summarized in Fig. 3. We build upon our earlier approach for graphene [35], adapting it for the case of CNT. Fig. 3a shows the energy changes with the addition of a new row of carbon atoms, dimer by dimer, for (6,6), (9,9) and (9,0) CNT. All three curves depart from the “nucleation to kink-flow” scenario of graphene, the reason being the constantly changing tilt angle of the CNT. However, both A curves (red, orange) show essentially the same height for the first dimer addition and the same maximum height (closer to the end). The Z curve bears the same qualitative character, having an initial and a final maximum. The maximum height of each curve determines the free energy barrier that needs to be overcome for successful addition of each new row of hexagons,  $\Delta G_A \approx 1.67$ – $1.86$  eV and  $\Delta G_Z > 3$  eV (calculations for the (9,0) CNT yield multiple intermediate structures with topo-

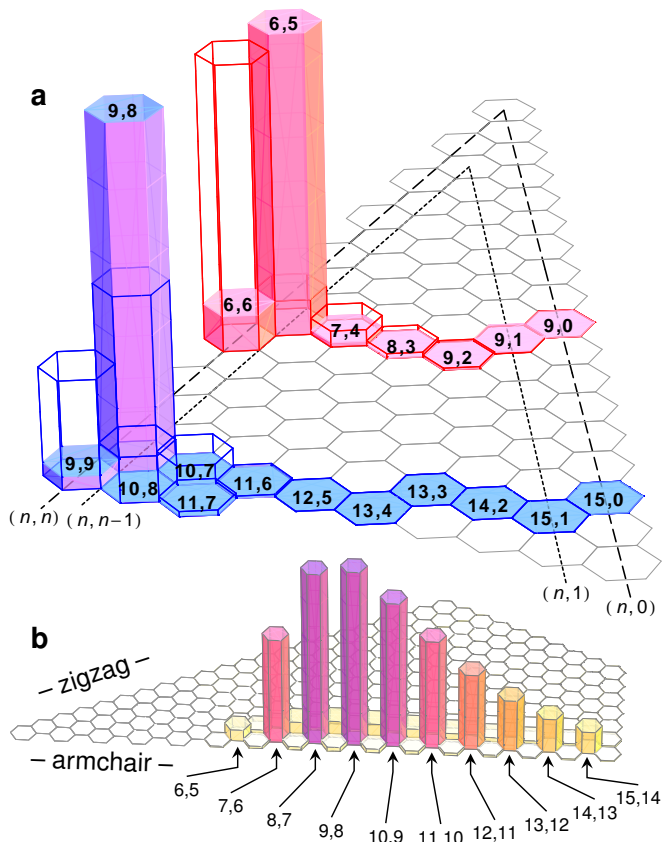


**Fig. 4. Predicted CNT type distributions.** (a) Distributions calculated directly based on MD computations for two CNT sets ( $d \approx 0.8$  nm and 1.2 nm, each distribution is normalized separately). The empty bars show chirality distributions for liquid catalyst case. (b) Full  $(n,m)$  distribution based on an analytical fit to MD interface energies. For all plots the temperature was artificially set to about three times the typical experimental value to make the heights visible.

logical defects of energies lower than perfect hexagonal structures, an additional complication for Z-CNT growth). These are the terms that penalize the pure A and Z tubes, compared to the chiral ones (green line in Fig. 3a), by an additional factor  $\propto e^{-\Delta G}$  and thus effectively remove them from the product distribution, despite their favorable cap-nucleation energies. The atomic configurations for the first dimer addition to the (6,6) and (9,0) CNT are shown in Fig. 3b. Fig. 3c shows the concentrations of different site types—Z, A, and K (kink)—as a function of  $\chi$ . Thin black lines show the intrinsic, topologically required values. Finally, Fig. 3d shows the CNT growth speed. Higher temperatures favor kink formation and promote the growth of zigzag and armchair CNT. However, under realistic conditions, when  $k_B T \ll \Delta G$ , the growth rate of achiral CNT is negligible. Among different diameters  $d$ , the curvature of the wall penalizes insertion of C atoms into small-diameter CNT, as in Eq. 2.

We now have all the ingredients to calculate the relative abundance of different CNT types. The distributions for the two CNT data sets in Fig. 4a both show a strong predomi-

nance of  $(n, n-1)$  near-armchair CNT. The selectivity of distributions is actually so strong that one has to increase the temperature to  $T = 2700$  K when plotting these distributions; at  $T = 900$  K, both show effectively single peaks for (6,5) or (9,8) CNT. Further, one can use either data set to compute a general  $(n,m)$  distribution through interface energy fitting. An example is shown in Fig. 4b. The peak in diameter distribution results from the competition between the interface energy, favoring smaller  $d$  in Eq. 1, and a prefactor due to the configurational entropy of CNT caps [33, 44], favoring larger diameters [2], which scales approximately as  $\sim d^8$  [45]. In a real CVD experiment, there will be additional constraints on  $d$ , from the size of catalyst particles. Then the product distribution will be a slice of Fig. 4b with prominent  $(n, n-1)$  peaks, such as those shown in Fig. 4a.

By similar logic, our theory suggests a possibility to highly selectively achieve the near-Z  $(n, 1)$  CNT, if a catalyst favors Z interface over A. While  $(n, n-1)$  are always semiconducting, the  $(n, 1)$  series contains all three CNT families (metallic and two semiconducting). Then, a control of diameter would allow a selective synthesis of CNT of either conductivity type. Moreover, when speculating on a possibility of catalyst-template exactly matching a certain  $(n,m)$  tube, we learn here that this would more likely favor the *one-index-off* tubes  $(n, m \pm 1)$ , to allow for rapid kinetics at the cost of somewhat higher energy of the contact and nucleation.

We can also compare the simulated distributions to a liquid catalyst model (dashed-dotted line in Fig. 2a and the kink formation energy  $E_A = 0$  [5]). The results are shown in Fig. 4a as hollow bars and display much greater presence of armchair CNT in the overall broader distribution. In reality, irregular and highly mobile structure of liquid catalyst may flatten the energy landscape in Fig. 2a and thus further broaden the distribution. If  $E_A > 0$ , the fastest-growing tubes have  $\chi = 19.1^\circ$  (Fig. 3d), which corresponds to  $(2m, m)$  CNT. Finally, with  $\chi$ -unbiased nucleation probability and  $E_A \rightarrow 0$ , one recovers the proportionality result,  $A \propto \chi$  [5].

In summary, the analysis above shows that the kinetic and thermodynamic aspects of CNT growth must be considered concurrently. The growth kinetics is aided by the kinks at the tube edge and thus favors the chiral types, in proportion to their chiral angle. The thermodynamic nucleation barrier, on solid catalyst, is lower for the kinkless edges of achiral tubes. In spite of complex and random variability of numerous atomic structures in the process, the overall product abundance can be summed up in a remarkably compact mathematical expression:  $x e^{-\beta \cdot x}$ . For lower temperatures and solid catalyst this function has a sharp maximum near zero, which explains the observations of near-armchair nanotubes in experiments. Higher  $T$  and liquid catalyst make contact energies relatively equal ( $\beta \rightarrow 0$ ) and nucleation of various types similarly probable, with the abundance then nearly proportional to chiral angle. This demonstrates that the approach is sufficiently comprehensive, being able to explain rather disparate facts accumulated over decades of experiments, from broader chiral distributions to very narrow, almost single type peaks.

Furthermore, we believe that the gained new insight must enable finding ways to engineer chiral-selective nanotube production, thus advancing variety of long-awaited applications, all pending availability of properly pure material.

**Acknowledgments:** Computer resources were provided by National Energy Research Scientific Computing Center, which is supported by the Office of Science of the U.S. Department of Energy under Contract No. DE-AC02-05CH11231; XSEDE, which is supported by NSF grant OCI-1053575, under allocation TG-DMR100029; and the DAVinCI cluster acquired with funds from NSF grant OCI-0959097.

\* These authors contributed equally.

† Correspondence to: [biy@rice.edu](mailto:biy@rice.edu)

- [1] Iijima, S. Helical microtubules of graphitic carbon. *Nature* **354**, 56–58 (1991).
- [2] Dresselhaus, M. S., Dresselhaus, G. & Eklund, P. C. *Science of fullerenes and carbon nanotubes* (Academic Press, San Diego, 1996).
- [3] Avouris, P., Chen, Z. & Perebeinos, V. Carbon-based electronics. *Nat. Nanotechnol.* **2**, 605–615 (2007).
- [4] De Volder, M. F. L., Tawfick, S. H., Baughman, R. H. & Hart, A. J. Carbon nanotubes: Present and future commercial applications. *Science* **339**, 535–539 (2013).
- [5] Ding, F., Harutyunyan, A. R. & Yakobson, B. I. Dislocation theory of chirality-controlled nanotube growth. *Proc. Natl. Acad. Sci. USA* **106**, 2506–2509 (2009).
- [6] Thess, A. *et al.* Crystalline ropes of metallic carbon nanotubes. *Science* **273**, 483–487 (1996).
- [7] Fouquet, M. *et al.* Highly chiral-selective growth of single-walled carbon nanotubes with a simple monometallic Co catalyst. *Phys. Rev. B* **85**, 235411 (2012).
- [8] Wang, H. *et al.* Chiral-selective CoSO<sub>4</sub>/SiO<sub>2</sub> catalyst for (9, 8) single-walled carbon nanotube growth. *ACS Nano* **7**, 614–626 (2013).
- [9] He, M. *et al.* Chiral-selective growth of single-walled carbon nanotubes on lattice-mismatched epitaxial cobalt nanoparticles. *Sci. Rep.* **3**, 1460 (2013).
- [10] Bachilo, S. M. *et al.* Structure-assigned optical spectra of single-walled carbon nanotubes. *Science* **298**, 2361–2366 (2002).
- [11] Bachilo, S. M. *et al.* Narrow (*n, m*)-distribution of single-walled carbon nanotubes grown using a solid supported catalyst. *J. Am. Chem. Soc.* **125**, 11186–11187 (2003).
- [12] Lolli, G. *et al.* Tailoring (*n, m*) structure of single-walled carbon nanotubes by modifying reaction conditions and the nature of the support of CoMo catalysts. *J. Phys. Chem. B* **110**, 2108–2115 (2006).
- [13] Li, X. *et al.* Selective synthesis combined with chemical separation of single-walled carbon nanotubes for chirality selection. *J. Am. Chem. Soc.* **129**, 15770–15771 (2007).
- [14] Harutyunyan, A. R. *et al.* Preferential growth of single-walled carbon nanotubes with metallic conductivity. *Science* **326**, 116–120 (2009).
- [15] Chiang, W.-H. & Sankaran, R. M. Linking catalyst composition to chirality distributions of as-grown single-walled carbon nanotubes by tuning Ni<sub>x</sub>Fe<sub>1-x</sub> nanoparticles. *Nat. Mater.* **8**, 882–886 (2009).
- [16] Liu, B., Ren, W., Li, S., Liu, C. & Cheng, H.-M. High temperature selective growth of single-walled carbon nanotubes with a narrow chirality distribution from a CoPt bimetallic catalyst. *Chem. Commun.* **48**, 2409–2411 (2012).
- [17] Zheng, M. *et al.* Structure-based carbon nanotube sorting by sequence-dependent DNA assembly. *Science* **302**, 1545–1548 (2003).
- [18] Tu, X., Manohar, S., Jagota, A. & Zheng, M. DNA sequence motifs for structure-specific recognition and separation of carbon nanotubes. *Nature* **460**, 250–253 (2009).
- [19] Scott, L. T. *et al.* A short, rigid, structurally pure carbon nanotube by stepwise chemical synthesis. *J. Am. Chem. Soc.* **134**, 107–110 (2012).
- [20] Mueller, A. & Amsharov, K. Y. Synthesis of precursors for large-diameter hemispherical buckybowls and precursors for short carbon nanotubes. *Eur. J. Org. Chem.* **2012**, 6155–6164 (2012).
- [21] Omachi, H., Nakayama, T., Takahashi, E., Segawa, Y. & Itami, K. Initiation of carbon nanotube growth by well-defined carbon nanorings. *Nat. Chem.* **5**, 572–576 (2013).
- [22] Ogrin, D. *et al.* Amplification of single-walled carbon nanotubes from designed seeds: Separation of nucleation and growth. *J. Phys. Chem. C* **111**, 17804–17806 (2007).
- [23] Orbaek, A. W., Owens, A. C. & Barron, A. R. Increasing the efficiency of single walled carbon nanotube amplification by Fe-Co catalysts through the optimization of CH<sub>4</sub>/H<sub>2</sub> partial pressures. *Nano Lett.* **11**, 2871–2874 (2011).
- [24] Liu, J. *et al.* Chirality-controlled synthesis of single-wall carbon nanotubes using vapour-phase epitaxy. *Nat. Commun.* **3**, 1199 (2012).
- [25] Shibuta, Y. & Maruyama, S. Molecular dynamics simulation of generation process of SWNTs. *Physica B: Condens. Matter* **323**, 187–189 (2002).
- [26] Ding, F., Bolton, K. & Rosén, A. Nucleation and growth of single-walled carbon nanotubes: A molecular dynamics study. *J. Phys. Chem. B* **108**, 17369–17377 (2004).
- [27] Zhao, J., Martinez-Limia, A. & Balbuena, P. B. Understanding catalysed growth of single-wall carbon nanotubes. *Nanotechnology* **16**, S575–S581 (2005).
- [28] Ribas, M. A., Ding, F., Balbuena, P. B. & Yakobson, B. I. Nanotube nucleation versus carbon-catalyst adhesion—probed by molecular dynamics simulations. *J. Chem. Phys.* **131**, 224501 (2009).
- [29] Amara, H., Bichara, C. & Ducastelle, F. Understanding the nucleation mechanisms of carbon nanotubes in catalytic chemical vapor deposition. *Phys. Rev. Lett.* **100**, 056105 (2008).
- [30] Page, A. J., Ohta, Y., Irle, S. & Morokuma, K. Mechanisms of single-walled carbon nanotube nucleation, growth, and healing determined using QM/MD methods. *Acc. Chem. Res.* **43**, 1375–1385 (2010).
- [31] Raty, J.-Y., Gygi, F. & Galli, G. Growth of carbon nanotubes on metal nanoparticles: A microscopic mechanism from *ab initio* molecular dynamics simulations. *Phys. Rev. Lett.* **95**, 096103 (2005).
- [32] Penev, E. S., Artyukhov, V. I., Ding, F. & Yakobson, B. I. Unfolding the fullerene: Nanotubes, graphene and poly-elemental varieties by simulations. *Adv. Mater.* **24**, 4956–4976 (2012).
- [33] Penev, E. S., Artyukhov, V. I. & Yakobson, B. I. Extensive energy landscape sampling of nanotube end-caps reveals no chiral-angle bias for their nucleation. *ACS Nano* **8**, 1899–1906 (2014).
- [34] Liu, Y., Dobrinsky, A. & Yakobson, B. I. Graphene edge from armchair to zigzag: The origins of nanotube chirality? *Phys. Rev. Lett.* **105**, 235502 (2010).

- [35] Artyukhov, V. I., Liu, Y. & Yakobson, B. I. Equilibrium at the edge and atomistic mechanisms of graphene growth. *Proc. Natl. Acad. Sci. USA* **109**, 15136–15140 (2012).
- [36] Rao, R., Liptak, D., Cherukuri, T., Yakobson, B. I. & Maruyama, B. In situ evidence for chirality-dependent growth rates of individual carbon nanotubes. *Nat. Mater.* **11**, 213–216 (2012).
- [37] Kudin, K. N., Scuseria, G. E. & Yakobson, B. I. C<sub>2</sub>F, BN, and C nanoshell elasticity from *ab initio* computations. *Phys. Rev. B* **64**, 235406 (2001).
- [38] van Duin, A. C. T., Dasgupta, S., Lorant, F. & Goddard III, W. A. ReaxFF: A reactive force field for hydrocarbons. *J. Phys. Chem. A* **105**, 9396–9409 (2001).
- [39] Mueller, J. E., Van Duin, A. C. T. & Goddard III, W. A. Development and validation of ReaxFF reactive force field for hydrocarbon chemistry catalyzed by nickel. *J. Phys. Chem. C* **114**, 4939–4949 (2010).
- [40] Plimpton, S. J. Fast parallel algorithms for short-range molecular dynamics. *J. Comput. Phys.* **117**, 1–19 (1995).
- [41] Aktulga, H. M., Fogarty, J. C., Pandit, S. A. & Grama, A. Y. Parallel reactive molecular dynamics: Numerical methods and algorithmic techniques. *Parallel Comput.* **38**, 245–259 (2012).
- [42] Giannozzi, P. *et al.* QUANTUM ESPRESSO: a modular and open-source software project for quantum simulations of materials. *J. Phys.: Condens. Matter* **21**, 395502 (2009).
- [43] Klein, D. Graphitic polymer strips with edge states. *Chem. Phys. Lett.* **217**, 261–265 (1994).
- [44] Brinkmann, G., Fowler, P., Manolopoulos, D. & Palser, A. A census of nanotube caps. *Chem. Phys. Lett.* **315**, 335–347 (1999).
- [45] Reich, S., Li, L. & Robertson, J. Structure and formation energy of carbon nanotube caps. *Phys. Rev. B* **72**, 165423 (2005).